The shape of the mitral annulus: A hypothesis of mechanical morphogenesis

The shape of the mitral annulus: a hypothesis of mechanical morphogenesis

D. Ambrosi* L. Deorsola† S. Turzi‡ M. Zoppello§

September 24, 2023

Abstract

This paper investigates the role of mechanics in the morphogenesis of the annulus of the mitral valve. We represent the annulus in its embryonic stage as an elastic ring and we perform a mechanical simulation of the development process applying a distributed torque on the rod: because of the mechanical action of the other growing cardiac chambers on the atrio-ventricular region, it departs from a planar circular shape. The numerical integration of the mathematical rod model subject to a bending load yields a shape very near to the one reported in the medical literature as anatomical reference for healthy patients.
To make the comparison quantitative, we illustrate a numerical approach to match two curves in 3D defining their distance in a proper mathematical way. Such a methodology is first applied to compare the annular shape resulting from the mechanical model with an anatomical reference "master" shape and it is then applied to set to clinical data extracted from MRI for a cohort of healthy patients. The good agreement among anatomical master description, numerical mechanical model and clinical data supports our speculation about a possible role of mechanics in determining the shape of the mitral valve.

1 Introduction

The cardiac valve which connects the left atrium to the left ventricle is known as Mitral Valve and allows blood to flow from the first cardiac chamber into the latter one, but not vice-versa. Even though this valve has a quite complex architecture, it can be essentially described as a structure formed by three components: the annulus, the leaflets and the subvalvular apparatus [1, 2]. The annulus is a ring with a specific three dimensional geometry: it exhibits a peculiar saddle shape, which is widely described in literature [3, 4, 1, 5, 6, 7].

The symmetric configuration of the valve ring allows us to identify two upper points and two lower ones (see figure 1). The first upper point is located in the middle of the anterior annulus, close to the Aortic valve, while the second one is placed on the opposite side, in the middle of the posterior annulus. These two points are called horns and the line connecting them, which is known as anteroposterior diameter, divides the valve annulus in two specular halves. Conversely, the two lower points of the annular perimeter are located sideways, at the level of the two valve commissures, that can be geometrically defined as the points with maximum distance from the symmetry axis. Even though the overall shape might appear quite complex, at a closer look it is can be effectively described as a circle bent upwards at the level of the intercommissural diameter.

Describing the valve annulus as a circle partially bent upwards, naturally leads to speculate about a possible explanation for the origin of its saddle shape during the embryonic heart development of the aortic valve [8, 9, 10]. To understand the mitral annular shape and its

*DISMA, Politecnico di Torino, corso Duca degli Abruzzi 24, 10129 Torino, Italy, davide.ambrosi@polito.it.
†Pediatric Cardiac Surgery Department, Ospedale Infantile Regina Margherita, Piazza Polonia 94, 10126 Torino, Italy, deorsola@libero.it.
‡Dipartimento di Matematica, Politecnico di Milano, Piazza Leonardo da Vinci 32, 20133 Milano, Italy, stefano.turzi@polimi.it
§DISMA, Politecnico di Torino, corso Duca degli Abruzzi 24, 10129 Torino, Italy marta.zoppello@polito.it.

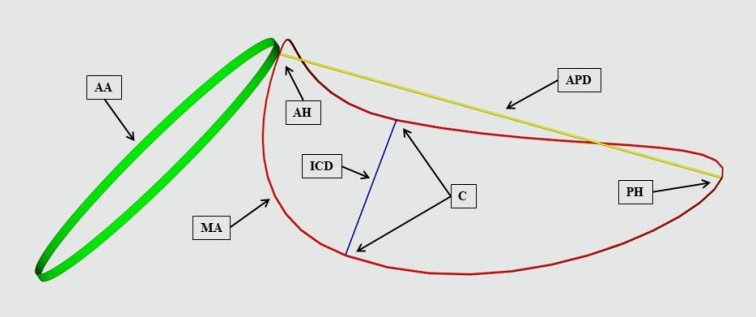

Figure 1: Sketch of the main geometrical features of the mitral annulus (red line) in contact with the aortic valve (green line): AA = Aortica Annulus, MA = Mitral Annulus, AH = Anterior Horn, PH = Posterior Horn, APD = Anteroposterior Diameter, C = Commissures, ICD = Intercommissural Diameter.

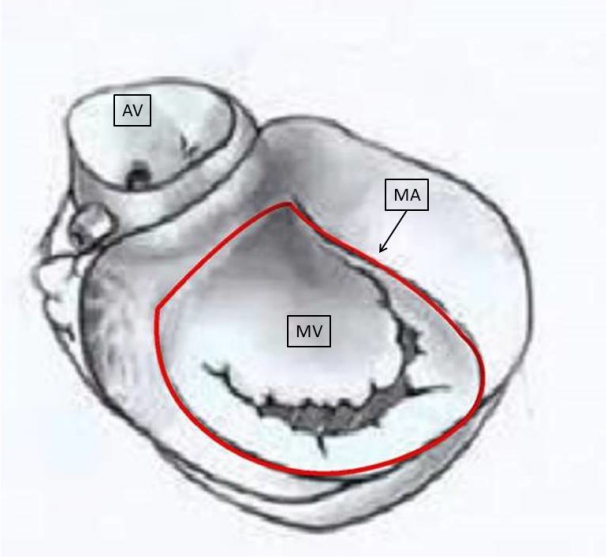

Figure 2: The stiffer aortic valve loads the softer mitral annulus that departs from its planar circular shape. Here: MV = Mitral Valve, AV = Aortic Valve, MA = Mitral Annulus.

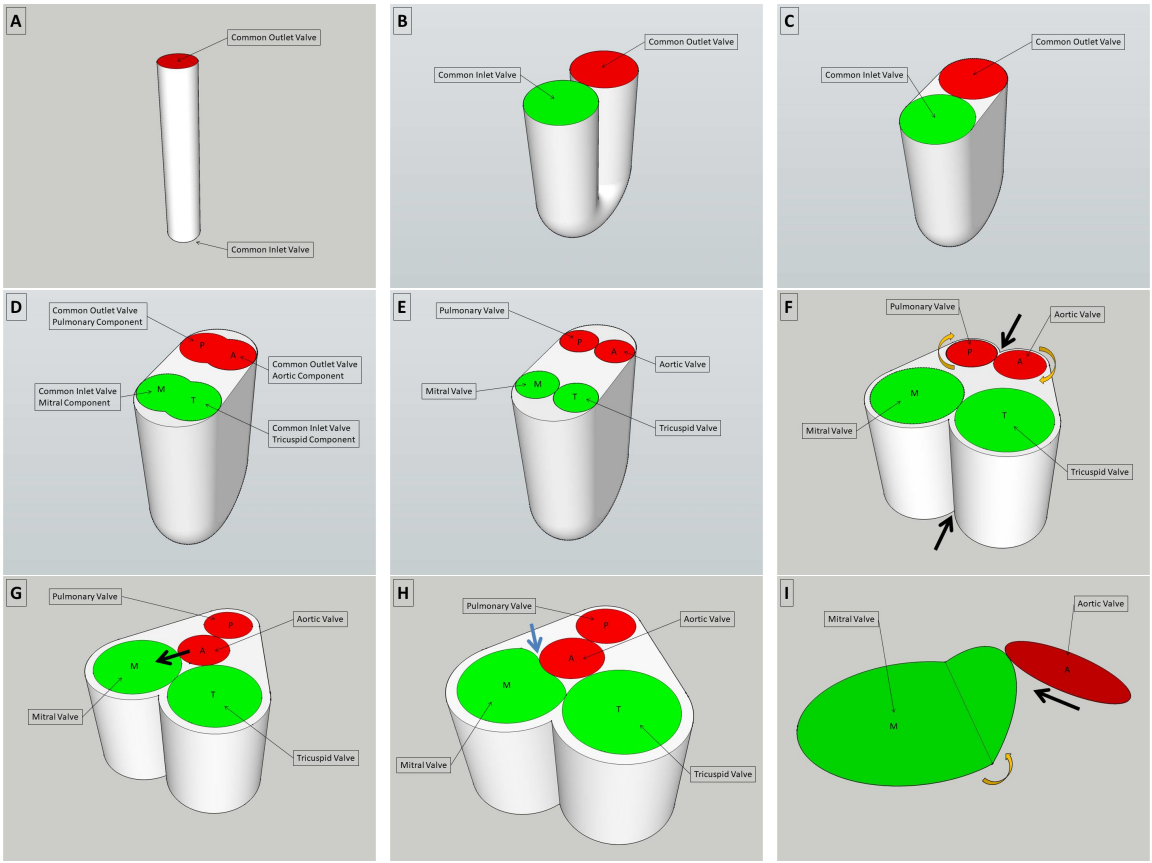

Figure 3: Sketch of the cardiac morphogenesis. The primordial cardiac tube bends and the separating wall is resorbed, then the original cardiac ends split into two valves that shift and rotate in a plane. When the mitral valve get in contact with the aortic valve they both exit from the plane and the former bends thus achieving the characteristic saddle shape.

spatial relationship with the aortic valve it is convenient to consider the most significant steps of the embryological cardiac development. Schematically speaking, we can identify eight main steps:

1. Originally the heart develops as a tube, with two valves located at its ends: a common inlet valve and a common outlet valve (Figure 1A).
2. The tube bends assuming a U shape, the lower end is displaced upper, thus positioning the two valves onto the same plane (Figure 1B).
3. The two vertical branches of the U shaped cardiac tube fuse together, creating a common cardiac sac: a structure which is going to divide again in two separate parts, one on the left and one on the right, creating the two cardiac ventricles. The two common valves are now both located within the base of the sac, which is commonly called cardiac base (Figure 1C).
4. Each common valve starts to subdivide in two separate components: the common inlet valve gives birth to the mitral and the tricuspid components, while the outlet common valve to the aortic and the pulmonary components (Figure 1D).
5. The common valve subdivision is now complete and within the base of the cardiac sac there are four valves: two inlets and two outlets. The inlet valves are represented by the mitral valve, on the left, and the tricuspid valve, on the right. Since the mitral valve will be the inlet of the left ventricle and the tricuspid valve the inlet of the right one, their location appears correct within the cardiac base. On the contrary, the positions of the aortic and the pulmonary valves result inverted, being the first the outlet of the left ventricle and the latter the outlet of the right one (Figure 1E).
6. To generate a correct connection between the two outlet valves and the two halves of the cardiac sac, which has already started to subdivide into the two cardiac ventricles, the two outlet valves undergo a 90 degrees clockwise rotation, which moves the aortic valve posteriorly and the pulmonary valve anteriorly (Figure 1F).
7. When the rotation is complete, the aortic valve occupies a characteristic position, located in the center of the cardiac base and wedged between the mitral and the tricuspid valves. Until this stage, the four cardiac valves are almost circular and lie on the same plane. Anyway, the aortic valve motion is not completed yet: the mitral valve keeps on shifting posteriorly and towards the left side of the cardiac base, pushing the anterior annulus of the mitral valve (Figure 1G).
8. As a result of such a migration, the mitral and the aortic valves exit the common former plane: they both bank and rise their common contact point, like the pitches of a roof. While the stiff aortic valve preserves a circular and planar shape, the softer mitral valve bends, taking its characteristic saddle shape (Figures 1H and 1I).

The existence of this morphogenetic mechanism is indirectly supported by the biomedical literature: it is reported that congenital malformations generating an incomplete rotation and no displacement, like described in the items above, yield a pathological planar and circular mitral valve [11, 12].

We show in this paper that a load of the aortic annulus modelled as an elastic ring can mechanically provide a deformation of the mitral annulus yielding a shape very similar to the one observed in nature. The curve generated by numerical simulation of rod bending are qualitatively very similar to the anatomical description. To make the comparison quantitative, we have elaborated a numerical algorithm based on the Procustes method that measures in a least squares sense the distance between two closed curves described by an arbitrary number of points with any orientation and scaling of the axis. A similar question has been addressed in [13] with a different approach: the geometrical characteristics of an annulus are stated on the basis of a number of standard geometrical quantities as area, circumference, anteroposterior diameter, commissural width, height. These geometrical indicators are usually compared with ranges obtained from clinical practice. Conversely, in this work we address the global geometrical shape of an annulus represented by a set of points with coordinates captured by echocardiography, in terms of distance between two curves. The shape of the mitral valve annulus, represented as a curve in 3D, is compared both versus a reference anatomical one and versus the results of mechanical simulations supported by developmental arguments.

2 Rod model

In this section the mitral annulus is mechanically represented as an inextensible and unshearable circular rod (a ring) subject to external forces and torques for a portion of its length. The external load accounts for the mechanical action of the adjacent growing chambers that bends the annulus, thus departing from the circular planar shape.

2.1 Kinematics

The centerline of our rod is a smooth curve $\mathbf{r}(s) : [0, L] \to \mathbb{R}^3$ parametrized by the arc length, in such a way that the vector tangent to the curve

$$d\mathbf{r}/ds = \mathbf{d}_1(s) \tag{1}$$

is a unit vector. We associate to $\mathbf{d}_1$ other two orthogonal material unit vectors $\mathbf{d}_2(s), \mathbf{d}_3(s)$, linked to the material properties of the cross section of the rod, so that $\mathbf{d}_1(s), \mathbf{d}_2(s), \mathbf{d}_3(s)$ define a local orthonormal right-handed basis [14]. In the special case that $\mathbf{d}_2$ is parallel to $d\mathbf{d}_1/ds$, we recover the Frénet basis and $\mathbf{d}_3$ is the binormal vector. However, we do not assume such a special orientation in the following.
The unit vectors of the local basis satisfy

$$\frac{d}{ds}\left(\mathbf{d}_1 \cdot \mathbf{d}_1\right) = \frac{d}{ds} 1 = 0 = 2\mathbf{d}_1' \cdot \mathbf{d}_1 \tag{2}$$

and so on, where we denote $\mathbf{d}_1' = d\mathbf{d}_1/ds$.
It follows that

$$\begin{aligned}
\mathbf{d}_1' &= (\mathbf{d}_1' \cdot \mathbf{d}_1)\mathbf{d}_1 + (\mathbf{d}_1' \cdot \mathbf{d}_2)\mathbf{d}_2 + (\mathbf{d}_1' \cdot \mathbf{d}_3)\mathbf{d}_3 = k_3\mathbf{d}_2 - k_2\mathbf{d}_3, \\
\mathbf{d}_2' &= (\mathbf{d}_2' \cdot \mathbf{d}_1)\mathbf{d}_1 + (\mathbf{d}_2' \cdot \mathbf{d}_2)\mathbf{d}_2 + (\mathbf{d}_2' \cdot \mathbf{d}_3)\mathbf{d}_3 = -k_3\mathbf{d}_1 + k_1\mathbf{d}_3, \\
\mathbf{d}_3' &= (\mathbf{d}_3' \cdot \mathbf{d}_1)\mathbf{d}_1 + (\mathbf{d}_3' \cdot \mathbf{d}_2)\mathbf{d}_2 + (\mathbf{d}_3' \cdot \mathbf{d}_3)\mathbf{d}_3 = k_2\mathbf{d}_1 - k_1\mathbf{d}_2,
\end{aligned} \tag{3}$$

where $k_1(s), k_2(s), k_3(s)$ describe the rotation rate of the unit vectors of the local basis $(\mathbf{d}_1, \mathbf{d}_2, \mathbf{d}_3)$ moving along the curve. For the Frénet basis, $k_2 = 0$, k_1 is the centerline curvature and k_3 is the geometrical torsion. In matrix form

$$\begin{pmatrix} \mathbf{d}_1' \\ \mathbf{d}_2' \\ \mathbf{d}_3' \end{pmatrix} = \begin{pmatrix} 0 & k_3 & -k_2 \\ -k_3 & 0 & k_1 \\ k_2 & -k_1 & 0 \end{pmatrix} \begin{pmatrix} \mathbf{d}_1 \\ \mathbf{d}_2 \\ \mathbf{d}_3 \end{pmatrix} = \mathbf{\Omega} \begin{pmatrix} \mathbf{d}_1 \\ \mathbf{d}_2 \\ \mathbf{d}_3 \end{pmatrix} \tag{4}$$

where the skew–symmetric $\mathbf{\Omega}$ at the right hand side represents the infinitesimal rotation of the basis. It can be rewritten as the product of two matrices

$$\mathbf{\Omega} = \mathbf{R}'\mathbf{R}^T \tag{5}$$

where $\mathbf{R}$ is the finite rotation of the reference basis into the actual one and the symbol ^{T} denotes transposition.
Summarizing: if the rotation rates (k_1, k_2, k_3) are known, given a suitable initial condition, the current basis $(\mathbf{d}_1, \mathbf{d}_2, \mathbf{d}_3)$ can be obtained by numerical integration of equation (4) and integration of equation (1) yields the actual configuration of the curve $\mathbf{r}(s)$. The orientation of the vector basis in the reference configuration, say $(\mathbf{d}_1^o, \mathbf{d}_2^o, \mathbf{d}_3^o)$ is related to the current basis $(\mathbf{d}_1(s), \mathbf{d}_2(s), \mathbf{d}_3(s))$ by application of the orthogonal matrix $\mathbf{R}$ [15]. As a matter of fact, the force and momentum balance equations to be introduced in the next section are written in terms of the k_is.

2.2 Elastic energy and balance equations

An inextensible and unshearable slender body is here represented by a rod: a one–dimensional manifold embedded in the three-dimensional space. The deformation of a rod can be defined as the superposition of three independent motions: bending in two (local) planes and twist of the rod along its own direction.
Bending along three axis is kinematically represented by the curvature, the derivative of the tangent vector $\mathbf{d}_1'(s)$. For a planar deformation this quantity is the inverse of the radius

of the disc locally tangent to the rod: the more rapidly $\mathbf{d}_1$ changes direction versus the curvilinear coordinate, the larger is the curvature. In terms of infinitesimal rotation $\mathbf{\Omega}$, we define the squared curvature of a rod that is in its relaxed state in the reference configuration as $\kappa^2 = |\mathbf{d}_1'|^2 = k_2^2 + k_3^2$. The reference configuration might not be the relaxed one, as in the case of our interest, and natural bending and torsion are to be included in the energetic description.
The twist of the beam is represented by the rotation of a vector normal to the rod (say $\mathbf{d}_3$) around the direction of the rod itself: in this case $\tau^2 = |\mathbf{d}_3'|^2 - (\mathbf{d}_3' \cdot \mathbf{d}_1)^2 = k_1^2$, where the component of $\mathbf{d}_3'$ along $\mathbf{d}_1$ is not considered since it gives no contribution to the torsion [16]. We assume that the elastic energy of the rod depends quadratically on its total curvature and twist obtained by integration along the curve:

$$W = \int_0^L \frac{\alpha}{2}(k_2 - k_{2o})^2 \, ds + \int_0^L \frac{\alpha}{2}(k_3 - k_{3o})^2 \, ds + \int_0^L \frac{\beta}{2}(k_1 - \tau_o)^2 \, ds \tag{6}$$

where k_{1o}, k_{2o} and τ_o are the natural bendings and torsion, respectively: the curvatures and twist that the rod owns in its own relaxed configuration (possibly different from the reference one). The bending modulus α and the torsion modulus β depend on the material and geometrical characteristics of the rod as follows:

$$\alpha = EI, \qquad \beta = GJ, \tag{7}$$

where E is the Young modulus of the material, G is the shear modulus, I is the moment of inertia of the rod and J is the axial moment. For the circular section we consider $J = 2I$, while the assumption of incompressibility yields $G = E/3$ [17], so that eventually $\beta = \frac{2}{3}\alpha$.
The left hand side of equation (6) can be rewritten in terms of the directors $\mathbf{d}_1$ and $\mathbf{d}_3$ using equations (3). Taking $\tau_o = 0$ we consider a planar circle as reference relaxed configuration and we get

$$\begin{aligned} W &= \int_0^L \frac{\alpha}{2}(k_2 - k_{2o})^2 \, ds + \int_0^L \frac{\alpha}{2}(k_3 - k_{3o})^2 \, ds + \int_0^L \frac{\beta}{2} k_1^2 \, ds \\ &= \int_0^L \frac{\alpha}{2}(-\mathbf{d}_1' \cdot \mathbf{d}_3 - k_{2o})^2 ds + \int_0^L \frac{\alpha}{2}(\mathbf{d}_1' \cdot \mathbf{d}_2 - k_{3o})^2 ds + \int_0^L \frac{\beta}{2}(\mathbf{d}_2 \cdot \mathbf{d}_3')^2 ds. \end{aligned} \tag{8}$$

Before proceedings with calculations, we notice that for variations of the basis ($\mathbf{d}_1$, $\mathbf{d}_2$, $\mathbf{d}_3$) the incremental directors should remain mutually orthonormal, and therefore the admissible variations of the basis are of the form

$$\begin{aligned} \delta\mathbf{d}_1 &= \mathbf{d}_2 \, \delta\eta_3 - \mathbf{d}_3 \, \delta\eta_2, \\ \delta\mathbf{d}_2 &= \mathbf{d}_3 \, \delta\eta_1 - \mathbf{d}_1 \, \delta\eta_3, \\ \delta\mathbf{d}_3 &= \mathbf{d}_1 \, \delta\eta_2 - \mathbf{d}_2 \, \delta\eta_1, \end{aligned} \tag{9}$$

where $\delta\eta_i$ are arbitrary non dimensional coefficients [18]. The coefficients $\eta_i, i = 1, 3$ should not be confused with the non-null components of the skew symmetric matrix $\mathbf{\Omega}$: the latter provide the rate of rotation of the directors as a function of the curvilinear coordinate, the former are arbitrary independent rotation of the directors that allow to identify the differential equations ensuring stationarity of the energy functional.
After appending the inextensibility and unshearability constraint (1) to the energy, we can write the principle of virtual work

$$\delta\hat{W}(k_1, k_2, k_3, \mathbf{N}, \mathbf{r}) = \delta\left(W(k_1, k_2, k_3) - \int_0^L \mathbf{N} \cdot (\mathbf{r}' - \mathbf{d}_1) ds\right) = \int_0^L \left(\mathbf{f} \cdot \delta\mathbf{r} + \sum_1^3 m_i \delta\eta_i\right) ds \tag{10}$$

where the Lagrange multiplier $\mathbf{N}(s)$ is the reaction force times length (the tension of the rod) to the constraint $\mathbf{r}' = 1$, $\mathbf{f}(s)$ and $\mathbf{m}(s) = (m_1, m_2, m_3)$ are the active force and torque linear density externally applied to the rod, represented in spatial coordinates, and $\delta\eta_i$, $i = 1, 2, 3$ are the entries of the skew-symmetric matrix defining the admissible variations of the basis ($\mathbf{d}_1$, $\mathbf{d}_2$, $\mathbf{d}_3$) in (9). One might notice that $\mathbf{N}$ and $\mathbf{m}$ have the same physical dimensions, upper

and lowercase denoting reactive and active forces, respectively. The tension $\mathbf{N}$ is represented in its spatial form

$$\mathbf{N} = \sum_{1}^{3} N_i \mathbf{d}_i. \tag{11}$$

After first variation of the energy W, we get

$$\delta W = \int_0^L \alpha(-\mathbf{d}_1' \cdot \mathbf{d}_3 - k_{2o})\delta(-\mathbf{d}_1' \cdot \mathbf{d}_3) ds + \int_0^L \alpha(\mathbf{d}_1' \cdot \mathbf{d}_2 - k_{3o})\delta(\mathbf{d}_1' \cdot \mathbf{d}_2) ds + \int_0^L \beta(\mathbf{d}_2' \cdot \mathbf{d}_3)\delta(\mathbf{d}_2' \cdot \mathbf{d}_3) ds. \tag{12}$$

Variation of products and integration by parts yields

$$\begin{aligned} \delta W = & \int_0^L \alpha \left((-\mathbf{d}_1' \cdot \mathbf{d}_3 - k_{2o})\mathbf{d}_3\right)' \cdot \delta \mathbf{d}_1 \, ds - \int_0^L \alpha(-\mathbf{d}_1' \cdot \mathbf{d}_3 - k_{2o})\mathbf{d}_1' \cdot \delta \mathbf{d}_3 \\ & - \int_0^L \alpha \left((\mathbf{d}_1' \cdot \mathbf{d}_2 - k_{3o})\mathbf{d}_2\right)' \cdot \delta \mathbf{d}_1 \, ds + \int_0^L \alpha(\mathbf{d}_1' \cdot \mathbf{d}_2 - k_{3o})\mathbf{d}_1' \cdot \delta \mathbf{d}_2 \, ds \\ & - \int_0^L \beta((\mathbf{d}_2' \cdot \mathbf{d}_3)\mathbf{d}_3)' \cdot \delta \mathbf{d}_2 \, ds + \int_0^L \beta(\mathbf{d}_2' \cdot \mathbf{d}_3)\, \mathbf{d}_2' \cdot \delta \mathbf{d}_3 \, ds + \text{boundary terms}. \end{aligned} \tag{13}$$

We rewrite equation (13) in terms of the components of the infinitesimal rotation matrix using (4):

$$\begin{aligned} \delta W = & -\alpha \int_0^L ((-(k_3\mathbf{d}_2 - k_2\mathbf{d}_3) \cdot \mathbf{d}_3 - k_{2o})\mathbf{d}_3)' \cdot \delta \mathbf{d}_1 \, ds \\ & - \alpha \int_0^L (-(k_3\mathbf{d}_2 - k_2\mathbf{d}_3) \cdot \mathbf{d}_3 - k_{2o})(k_3\mathbf{d}_2 - k_2\mathbf{d}_3) \cdot \delta \mathbf{d}_3 \, ds \\ & - \alpha \int_0^L (((k_3\mathbf{d}_2 - k_2\mathbf{d}_3) \cdot \mathbf{d}_2 - k_{3o})\mathbf{d}_2)' \cdot \delta \mathbf{d}_1 \, ds \\ & + \alpha \int_0^L ((k_3\mathbf{d}_2 - k_2\mathbf{d}_3) \cdot \mathbf{d}_2 - k_{3o})(k_3\mathbf{d}_2 - k_2\mathbf{d}_3) \cdot \delta \mathbf{d}_2 \, ds \\ & - \beta \int_0^L (((k_1\mathbf{d}_3 - k_3\mathbf{d}_1) \cdot \mathbf{d}_3)\mathbf{d}_3)' \cdot \delta \mathbf{d}_2 \, ds \\ & + \beta \int_0^L ((k_1\mathbf{d}_3 - k_3\mathbf{d}_1) \cdot \mathbf{d}_3)(k_1\mathbf{d}_3 - k_3\mathbf{d}_1) \cdot \delta \mathbf{d}_3 \, ds + \text{b.t.} \\ = & \alpha \int_0^L ((k_2 - k_{2o})\mathbf{d}_3)' \cdot \delta \mathbf{d}_1 \, ds - \alpha \int_0^L (k_2 - k_{2o})(k_3\mathbf{d}_2 - k_2\mathbf{d}_3) \cdot \delta \mathbf{d}_3 \, ds \\ & - \alpha \int_0^L ((k_3 - k_{3o})\mathbf{d}_2))' \cdot \delta \mathbf{d}_1 \, ds + \alpha \int_0^L (k_3 - k_{3o})(k_3\mathbf{d}_2 - k_2\mathbf{d}_3) \cdot \delta \mathbf{d}_2 \, ds \\ & - \beta \int_0^L (k_1\mathbf{d}_3)' \cdot \delta \mathbf{d}_2 \, ds + \beta \int_0^L k_1(k_1\mathbf{d}_3 - k_3\mathbf{d}_1) \cdot \delta \mathbf{d}_3, ds + \text{b.t.} \end{aligned} \tag{14}$$

Using now the admissible variations formula (9), after some algebraic manipulations we get

$$\begin{aligned} \delta W = \alpha \int_0^L & (-k_2'\delta\eta_2 - k_1(k_2 - k_{2o})\delta\eta_3 + k_3(k_2 - k_{2o})\delta\eta_1 \\ & - k_3'\delta\eta_3 + k_1(k_3 - k_{3o})\delta\eta_2 - k_2(k_3 - k_{3o})\delta\eta_1)\, ds \\ + \beta \int_0^L & \left(-k_1'\delta\eta_1 + k_1k_2\delta\eta_3 - k_3k_1\delta\eta_2\right) ds + \text{b.t.}. \end{aligned} \tag{15}$$

First variation and integration by parts of the inextensibility constraints in (10) yields

$$\begin{aligned} & -\int_0^L \delta\mathbf{N} \cdot (\mathbf{r}' - \mathbf{d}_1) ds - \int_0^L \mathbf{N} \cdot \delta\mathbf{r}' ds + \int_0^L \mathbf{N} \cdot \delta\mathbf{d}_1 \, ds = \\ & \quad - \int_0^L \delta\mathbf{N} \cdot (\mathbf{r}' - \mathbf{d}_1)\, ds + \mathbf{N} \cdot \mathbf{r}\big|_0^L + \int_0^L \mathbf{N}' \cdot \delta\mathbf{r}\, ds + \int_0^L \mathbf{N} \cdot (-\mathbf{d}_2\delta\eta_3 + \mathbf{d}_3\delta\eta_2)\, ds, \end{aligned} \tag{16}$$

where the notation $\mathbf{n}'$ denotes the Poisson derivation rule applied to the spatial vector $\mathbf{N}$ as obtained using equations (11) and (4).
As the arguments of the constrained energy $\hat{W}(k_1, k_2, k_3, \mathbf{N}, \mathbf{r})$ vary independently, equation (10) rewritten in terms of explicit first variation as in equations (15) and (16) can only hold if the following Euler–Lagrange equations apply.

$$\mathbf{N}' = \mathbf{f}, \tag{17a}$$
$$\beta k_1' + \alpha(k_3 k_{2o} - k_2 k_{3o}) + m_1 = 0, \tag{17b}$$
$$\alpha k_2' - k_1 k_3(\alpha - \beta) + \alpha k_1 k_{3o} + m_2 + N_3 = 0, \tag{17c}$$
$$\alpha k_3' + k_1 k_2(\alpha - \beta) - \alpha k_1 k_{2o} + m_3 - N_2 = 0, \tag{17d}$$
$$(\mathbf{d}_1', \mathbf{d}_2', \mathbf{d}_3')^T = \mathbf{\Omega}\,(\mathbf{d}_1, \mathbf{d}_2, \mathbf{d}_3)^T \tag{17e}$$
$$\mathbf{r}' = \mathbf{d}_1. \tag{17f}$$

Equations (17a), (17b), (17c) and (17d) denote balance of force, torque and bending moment, respectively. Equation (17e) accounts for the rotation of the local basis versus the curvilinear coordinate. Equation (17f) enforces the inextensibility and unshearability constraint. Balance equations are to be supplemented by 18 boundary conditions that naturally show up when applying the variational procedure: we detail them for the specific case of interest in this paper in the next section.

Remark 1 In the mechanical literature the balance equations (17) are often directly introduced, without going through a lengthy variational derivation. However, in the presence of constraints, as the inextensibility and unshearability constraints we assume, the derivation of the balance equations from a variational principle is, in our opinion, more transparent and physically motivated.

3 The mitral valve annulus as a loaded circular rod

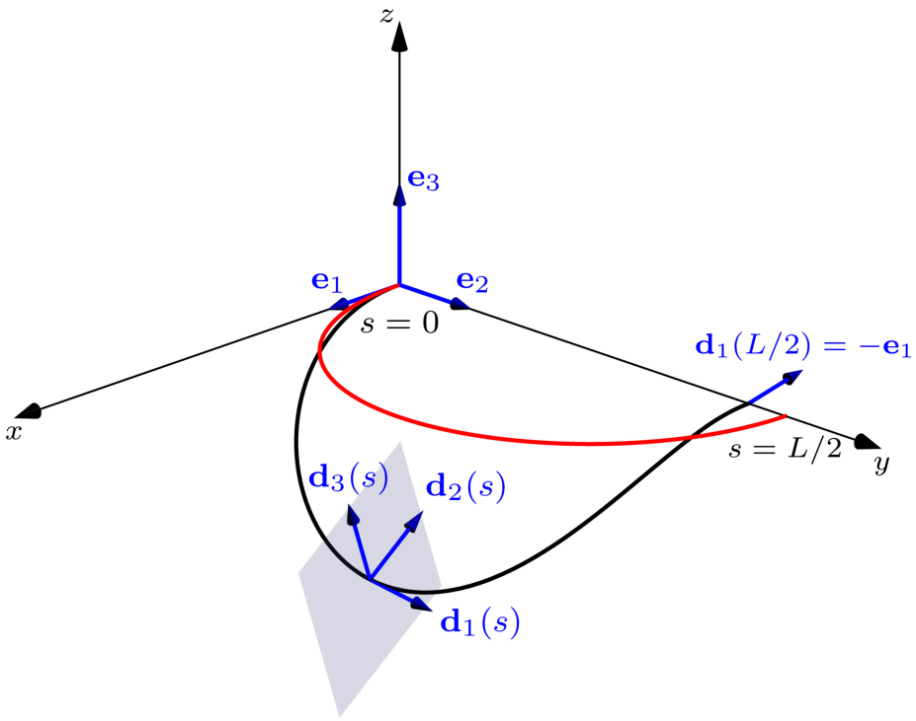

Figure 4: The circular unloaded configuration of the mitral annulus (black) and the deformed one (red).

We represent the mitral valve annulus as a circular rod of length L, with null residual elastic energy: the body is relaxed in its circular configuration, while the reference configuration is the straight one. The natural torsion is therefore $\tau_o = 0$ while the natural bending is $k_{2o} = 0, k_{3o} = \mathbf{d}_1' \cdot \mathbf{d}_2 = |\mathbf{d}_1'| = (2\pi)/L$.
To solve equations (17), the differential system has to be complemented by a suitable set of boundary conditions. As the mitral annulus is a closed curve, continuity conditions can be defined on the boundary for all the fields. We chose a different strategy, based on the observation that the anterior–posterior segment defines an axis of symmetry for the valve. We therefore restrict our numerical model to half length of the annulus. The annulus at rest is in the (x, y) plane and the posterior saddle horn is placed in the origin of the axis. The following boundary conditions apply (see figure 1):

$$\mathbf{r}(0) = (0, 0, 0), \tag{18a}$$

$$\mathbf{d}_1(0) = (1, 0, 0), \mathbf{d}_2(0) = (0, 1, 0), \mathbf{d}_3(0) = (0, 0, 1) \tag{18b}$$

$$x(L/2) = 0, z(L/2) = 0, k_1(L/2) = 0, d_1, 1(L/2) = -1, d_1, 2(L/2) = 0, \tag{18c}$$

where $d_1, 1$ and $d_1, 2$ denote the first two components of the unit vector $\mathbf{d}_1$. Without explicit imposition, the third one is automatically null because of the dynamics enforced by equation (5): if $\mathbb{R}$ is orthogonal at $s = 0$, $\mathbb{R}(s)$ is orthogonal for every s. As a consequence, the columns of $\mathbb{R}$ are unit vectors for every value of the curvilinear coordinate and enforcing two components of $\mathbf{d}_1$ in $s = L/2$ is sufficient to provide information on the whole unit vector.
One more boundary condition is needed. In $s = L/2$ the y coordinate of the boundary point is not constrained, and therefore no reaction force applies in such a direction. In rotated coordinates the condition reads:

$$\mathbf{N}(L/2) \cdot \mathbf{d}_2^o = \mathbf{N}(L/2) \cdot \mathbf{R}^T \mathbf{d}_2 = 0. \tag{19}$$

The torque $\mathbf{M}(s)$ is applied on the portion of the rod corresponding to the saddle, bounded by the commissures in Figure (1). It represents the load of the aortic valve that bends the annulus during development, thus departing from the circular shape.

Remark 2 While we are not aware of mechanical literature discussing the mechanical properties of the mitral annulus on an experimental basis, it is known from clinical data that it undergoes 23-40% variation in circumference length between the systolic and diastolic configuration [19]. While this observation apparently suggests an assumption of extensibility, we have adopted an inextensibility constraint in our model. The argument for this assumption is that we do not apply any elongating force to the annulus: we only apply bending force and couple. It is well known that the energy needed to bend and an elastic rod is much smaller than the one needed to elongate it and therefore we assume that our mechanical loads do not generate any elongation in the rod, so that no elongation energy storage has to be included in the model.
Remark 3 In the same vein of the comment above, at our knowledge it is not reported in the biomechanical literature if the mitral annulus relaxes residual stress when excided. It is not therefore known whether the saddle-type shape or the annular form could be generated by residual stress produced by an inhomogeneous growth. In other words, the autonomous placement of the excised and cut annulus in a fully unconstrained and unloaded setting could provide information about the inner (growth) or outer (loads) nature of the shaping of the annulus. The former should be modelled by a suitable definition of the reference natural bending and twist k_{1o}, k_{2o} and τ_o, possibly depending in the curvilinear coordinate s. The latter is described by external loads, in terms of forces an torques. In the large existing anatomical literature are reported several figures of excised mitral valves, laying on a flat surface [20, 21, 22, 19, 23]. Most of the pictures display a flat structure with a rather homogeneous curvature. On the basis of such a very qualitative observation, we have decided to include in our model a natural bending corresponding to a flat relaxed circle (a ring). On the other hand, we are aware that the main interest of those pictorial representations was not mechanical, but anatomical, and this issue requires much deeper investigation. We only mention that mathematical modelling of pre-stressed biological materials is nowadays a consolidated area and the way to modify the model in terms of additive prestress or multiplicative prestrain is a well understood subject [24]. In this respect, an interplay between external loads and internal remodelling couples is very plausible and deserve further studies [25].

4 Compare shapes: the distance between two curves

The numerical integration of the mechanical morphogenetic model described in the previous section provides us with a curve, possibly described pointwise: an array of ordered positions. These results data extracted from echocardiography or CT scan of patients that are arrays of positions captured at different mutual distance, different placement of the origin of the axis and different spatial orientation. In order to make a significant comparison between curves, we apply the Procustes Method [26] that we detail and tailor below for our purposes.
We initially format the clinical data performing the following operations:

- approximate every pointwise curve by a spline, so that we have a smooth representation of every curve whatever is the number of the points used to define it;
- calculate the center of mass of every curve and translate it into the origin of the axis;
- calculate the length of each curve ℓ_i and re-parametrize it, so that each one has unitary length.

At this step, two curves must be oriented in a suitable way to make the comparison significant. We have in principle devised three possible approaches to provide such an orientation. The former approach is to utilize the axes of symmetry drawn by the radiologist, who identify the intercommissural and the anterior-posterior diameters that now read as the axis of symmetry of the patients valve to be aligned as the ones of the master valve. We have discarded this approach as it is operator–dependent (mainly for pathological valves) and we have then considered the possibility to calculate numerically the axis of symmetry of the curve represented by the principal axis of inertia of the curve (ordered according to the eigenvalues). Unfortunately, this methodology amplifies the noise that is unavoidably involved in the manual capture of coordinates and the axis of symmetry, even in the case of healthy valves, can be poorly reproduced.
Our final methodological choice is to look for the orthogonal transformation (including both rotations and reflections) that minimises the distance between the two curves. Formally, let $\hat{\mathbf{p}}(s)$ and $\mathbf{p}(s)$) are the unitary length parametric representations of the master and of the patient annulus as obtained at the end of the steps illustrated above. We look for the orthogonal matrix Q such that the L^2 distance between the curves

$$\hat{\mathcal{F}}(\mathsf{Q}) = \int_0^1 (\hat{\mathbf{p}}(s) - \mathsf{Q}\mathbf{p}(s))^2 ds, \tag{20}$$

is minimum. In a discrete representation this requirement corresponds to minimize

$$\mathcal{F}(\mathsf{Q}) = \sum_{j=1}^{n} (\hat{\mathbf{p}}_j - \mathsf{Q}\mathbf{p}_j)^2, \tag{21}$$

where $\hat{\mathbf{p}}_j = \hat{\mathbf{p}}(s_j), \mathbf{p}_j = \mathbf{p}(s_j)$, The n nodes $0 \le s_j \le 1$ are equally spaced and the orthogonal matrix Q is such that $\mathsf{Q}^T\mathsf{Q} = \mathsf{Q}\mathsf{Q}^T = \mathsf{I}$.
Standard derivation of the functional $\mathcal{F}(\mathsf{Q})$ yields the equation

$$\sum_{j=1}^{n} (\hat{\mathbf{p}}_j - \mathsf{Q}\mathbf{p}_j) \cdot \delta\mathsf{Q}\mathbf{p}_j = 0. \tag{22}$$

As equation (22) must hold for any increment matrix $\delta\mathsf{Q}$, without enforcing at first its orthogonality, after transposition we get

$$\sum_{j=1}^{n} (\hat{\mathbf{p}}_j \mathbf{p}_j^T - \mathsf{Q}\mathbf{p}_j \mathbf{p}_j^T) = 0. \tag{23}$$

When defining

$$\mathsf{A} = \sum_{j=1}^{n} \hat{\mathbf{p}}_j \mathbf{p}_j^T \qquad \mathsf{B} = \sum_{j=1}^{n} \mathbf{p}_j \mathbf{p}_j^T, \tag{24}$$

we eventually get the matrix equation $\mathsf{Q}\mathsf{B} = \mathsf{A}$ or

$$\mathsf{Q} = \mathsf{A}\mathsf{B}^{-1}. \tag{25}$$

To enforce the requirement that Q is an orthogonal matrix, we calculate the singular value decomposition of the right hand side of equation (25)

$$\mathsf{A}\mathsf{B}^{-1} = \mathsf{V}\mathsf{S}\mathsf{U}^T, \tag{26}$$

where V and U are orthogonal and S is diagonal positive definite. The projection of $\mathsf{A}\mathsf{B}^{-1}$ on the space of the orthogonal matrices is therefore represented by $\mathsf{V}\mathsf{U}^T$ [27] and, finally, we define the squared distance

$$d = \frac{1}{n}\sqrt{\sum_{j=1}^{n}(\hat{\mathbf{p}}_j - \mathsf{V}\mathsf{U}^T\mathbf{p}_j)^2}. \tag{27}$$

Remark 4 In the present work we are deliberately adopting a sloppy definition of curve when we claim the aim to compare two "curves": as a matter of fact we are interested in comparing the support of two curves. Two closed curves can be actually different while sharing the same support if they have a different parametrization, different orientation or different initial points. The notion of distance inherent in equation (21) is independent of the parametrization because the unit length curves are subdivided in the same number of equal subintervals. However equations (21) is meaningful only if curves are defined starting from the same spatial position and with the same orientation. This is the case for the present work: clinical and master points have all been captured starting from the anterior horn and moving in clockwise orientation looking at the annulus from the atrium into the ventricle. However, we mention that even in the case of non homogeneous data, a meaningful definition can be recovered by a more expensive strategy, minimizing the functions $\mathcal{F}$ also among any possible starting point and any orientation of the curves, i.e. minimizing among all possible parameterizations. This is nothing but an L^2 version of the Fréchet distance, that is usually defined with the L^∞ norm [28].

5 Numerical results

Numerical integration of equations (17–17f) with boundary condition (18) and (19) has been addressed by the solver `Ndsolve` of Mathematica. The bending and stiffness non-dimensional elastic moduli are $\alpha = 1$ and $\beta = 0.8$, respectively. The distributed torque applied on the annulus is

$$\mathbf{M}(s) = -m\,\mathbf{d}_1^o\,g(s), \tag{28}$$

where $g(s) = 1$ is a Gaussian function with $\sigma = 0.05$ centered in $s = \frac{3}{4}$ and accounts for the clock-wise bending around the x axis produced by the impinging arterial valve.

Remark 4 The distributed torque adopted in equation (28) is the simplest load that can be applied to a mechanical system that is still so poorly understood. We modulate the magnitude of the torque to optimize the results of the numerical simulation versus digital data. A more realistic representation of the load produced by the arterial valve on the mitral annulus could be obtained by addressing a larger system, where the growth of the arterial valve is included. In such a framework, $\mathbf{M}$ would not be external to the annular system (and therefore to prescribe) but they would be internal to the aortic annulus-mitral annulus system (an unknown to be calculated). This represents a natural direction of development of the present work.

5.1 Mechanical versus anatomical shape

A comparison between the anatomical shape reported in clinical literature as canonical reference curve [2] and the shape obtained on the basis of the mechanical model illustrated in section 3 are reported in figure 5.1 The curves are in qualitative very good agreement; the only appreciable difference is in top portion of the saddle, which appears slightly more rounded from mechanical simulations than in the anatomical model. The quantitative comparison is also very good: the mean squared difference between the curves as defined in (27) is $d = 0.01026$. Such a numerical value has to be compared with the unit length of the curve, so it tells us that the average difference is about 1% the length.

The solution is robust versus the choice of the torque peak density illustrated in section 3. The weak dependence of the result versus the choice of the parameter is certified by the

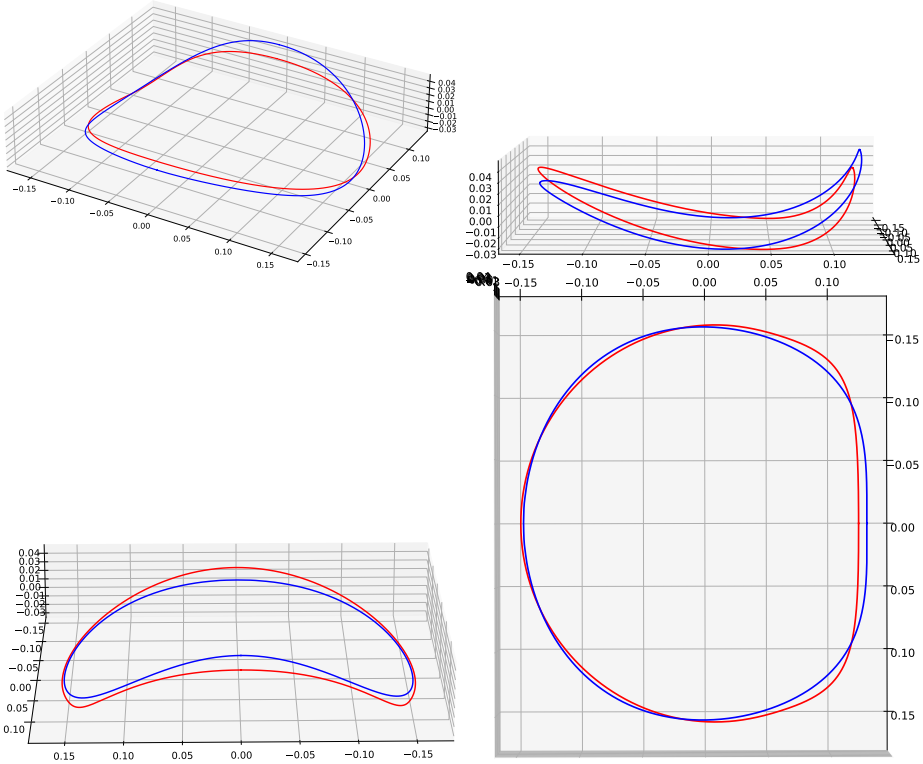

Figure 5: Several views of the curves representing the mitral annulus obtained by mechanical simulation (blu) and the one resulting from anatomical practice (red). The curves are in qualitative very good agreement except for top portion of the saddle, which appear more rounded from mechanical simulations than in real anatomy

.

plot in Figure 5.1, where the L2 error ϵ of the numerical solution compared with the reference one, is plotted versus the torque magnitude m. Around the optimal value $m = 4.04$ the curve is quite flat, then exhibiting a poor dependence of the solution on the estimated value; quantitatively speaking, around the optimal value we have

$$\frac{\Delta\epsilon}{\epsilon} \simeq 0.35 \frac{\Delta m}{m}. \tag{29}$$

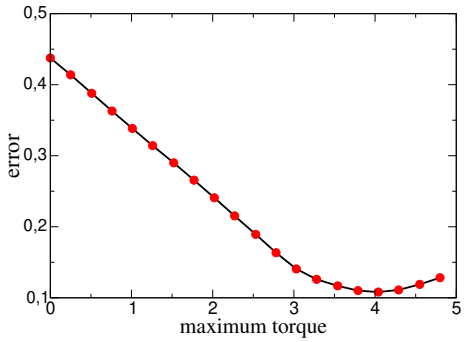

Figure 6: Plot of the difference between numerical and master curve (the "error") versus the maximum torque applied. The best fit of the data is obtained for $m = 4.04$; however the dependence of the result on the fitted parameter is weak, because the curve is quite flat around the minimum value.

5.2 Master anatomical versus clinical shape

A comparison between the anatomical reference shape and data extracted from TC scan for a single specific patient is reported in figure 5.2 The curves are in qualitative good agreement, except for undulations of the patient curve, a noise that could be expected. The mean squared difference between the curves defined as in (27) is $d = 0.01576$, slightly larger than the mechanical-to-master comparison. A more meaningful measure is obtained performing the same comparison with an average clinical curve extracted from a cohort of healthy adult patients. We define an average clinical mitral valve curve summing up all the curve supports of 26 patients after their reparametrization to unit length, displacement and optimal orientation. The mean quadratic distance between the average clinical curve and the master one is $d = 0.01476$ (see Figure 6). The averaging procedure suppresses the wiggles typically produced by the operator extracting the data from medical images (see Figure 5.2). This results tells us that the rod shape defined in the medical literature as a golden representative of the mitral valve annulus and the one obtained on the basis of mechanical loads can be considered an excellent representative of the real (average) valvular annulus.

Final Remarks

In this paper we have investigated a conjecture about the morphogenesis of the mitral valve annulus from a theoretical mechanics point of view. We speculate that the characteristic saddle shape of the annulus can be produced by the mechanical load applied by the aortic valve during the embryonic development. The mitral valve annulus is therefore mechanically represented as an elastic ring, a circular rod bended by an external load. We apply a distributed torque on the portion of contact annulus, to mimic with a least complexity the load produced by impinging aortic annulus. The good agreement between the shape predicted by the mechanical model and the master shape defined as standard in the anatomical literature supports our morphogenetic conjecture.
The good reproduction of the saddle shape of the mitral annulus in terms of applied load is of course not a proof of concept that excludes other morphogenetic mechanisms: most likely the

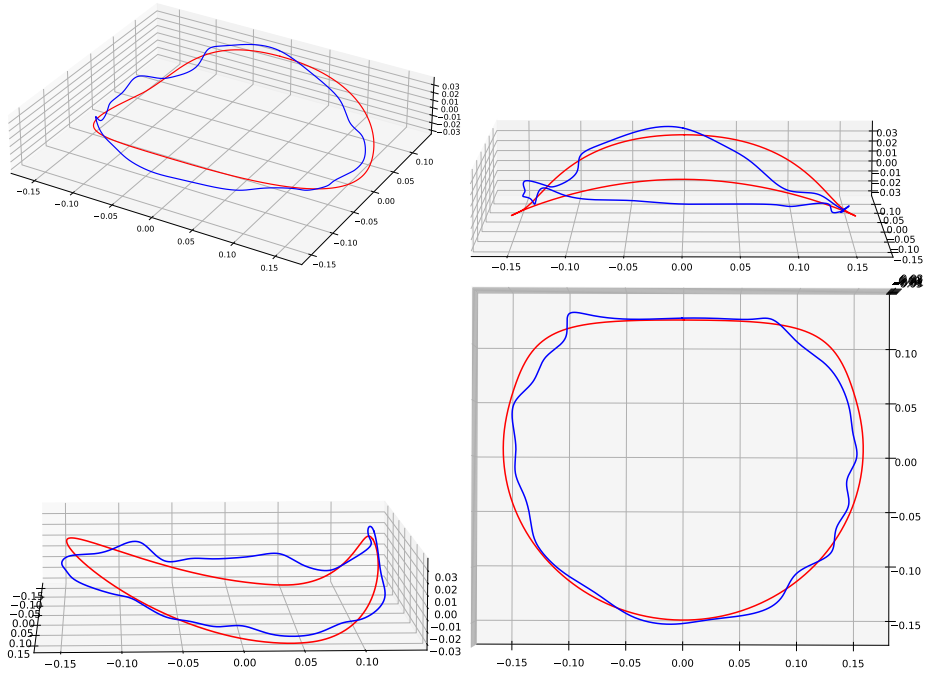

Figure 7: Side and top view of the curves representing the mitral annulus obtained by anatomical comparative studies (red) and one obtained by a single patient CT scan (blue). The curves are in qualitative very good agreement, the clinical one naturally exhibiting experimental noise.

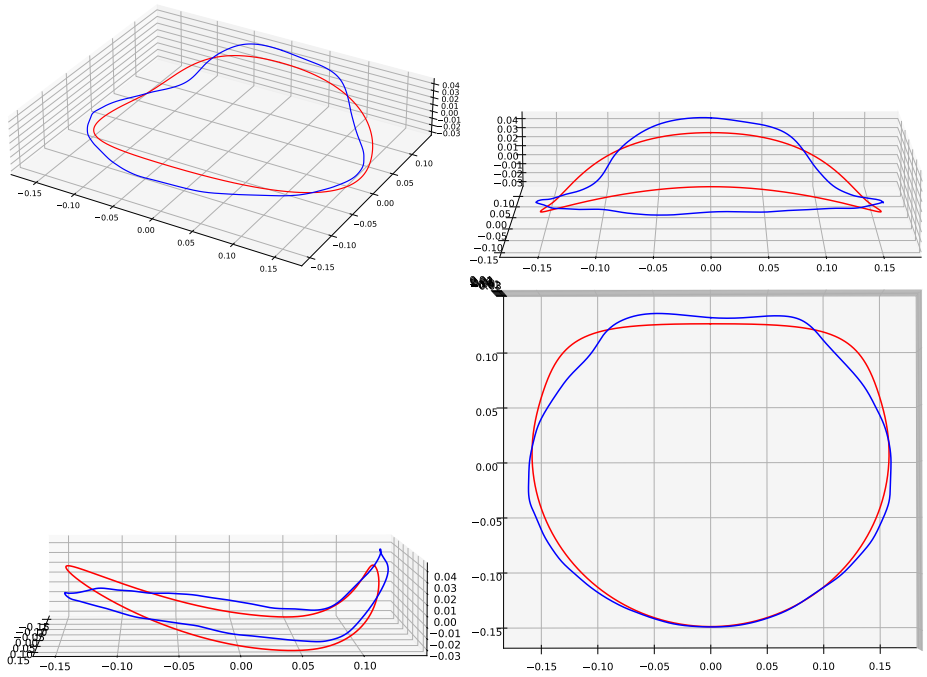

Figure 8: Several views of the curves representing the mitral annulus obtained by anatomical comparative studies (red) and the one obtained by average of a cohort of 26 patients CT scan (blue). The curves are in qualitative good agreement, the averaging procedure suppresses the operator–dependent wiggles.

mechanical action of the aortic ring during development is accompanied by a development of the tissue that is partially shaped by the external mechanical stimuli. The extraction from data of this kind of information requires quite a sophisticated measure of residual stress of very soft matter, as in the case of arterial layers [29], and it has not yet been applied to the mitral annulus. The theoretical representation of growth and remodelling of living matter is however nowadays a well understood subject [24], and we do not include this dynamics in the mathematical model only because of the lack of biomechanical information.
Our work is, at our knowledge, the first attempt to identify formally a role for mechanics in the mitral valve morphogenesis. Cardiac morphomechanics is still in its infancy and a limited number of studies have appeared in the mechanical literature (remarkable examples are [30] and [31]). The rod model adopted in the present work is a first step in the direction of a possible three dimensional modelling of the mitral valve attached to the ventricle, thus introducing a more realistic mechanical interaction of the annulus with the surrounding tissue. In the same vein, experimental data are needed to support or falsify the assumption of relaxed plane circular shape that we have adopted here on basis of extrapolation of medical images that had been captured for other aims.
Finally, a formal definition of the difference ("the distance") between two curves (their support, actually) has been needed to provide a quantitative support to the comparison. To this aim, we have developed a numerical method to compare in a precise mathematical sense the support of two closed curves, whatever is their parameterization. The methodology is successfully applied to compare anatomical master description with results of the numerical mechanical model, single patient and average clinical data. The effectiveness of the methodology suggests that our approach can be exploited in the future as a clinical tool to evaluate the degree of pathology of a mitral annulus.

Acknowledgments

We are indebted with Fabio Vicini for training us in Python. This work has been partially supported by the Indam-Gnfm.

References

[1] D Oliveira, J Srinivasan, D Espino, K Buchan, D Dawson, and D Shepherd. Geometric description for the anatomy of the mitral valve: a review. Journal of Anatomy, 237(2):209–224, 2020.

[2] L. Deorsola and A. Bellone. The golden proportion in the scallop geometry of normal mitral valves. when nature plays with jigsaw puzzles. Echocardiography, 36(6):1028–1034, 2019.

[3] LP Ryan, BM Jackson, Y Enomoto, L Parish, TJ Plappert, MGS John-Sutton, RC Gorman, and JH Gorman III. Description of regional mitral annular nonplanarity in healthy human subjects: a novel methodology. The Journal of Thoracic and Cardiovascular Surgery, 134(3):644–648, 2007.

[4] LP Ryan, BM Jackson, TJ Eperjesi, TJ Plappert, MSt John-Sutton, RC Gorman, and JH Gorman III. Quantitative description of mitral valve geometry using real-time three-dimensional echocardiography. Innovations, 2(5):237–244, 2007.

[5] MA Jolley, SJ Ghelani, A Adar, and DM Harrild. Three-dimensional mitral valve morphology and age-related trends in children and young adults with structurally normal hearts using transthoracic echocardiography. Journal of the American Society of Echocardiography, 30(6):561–571, 2017.

[6] AM Pouch, M Vergnat, JR McGarvey, G Ferrari, BM Jackson, CM Sehgal, PA Yushkevich, RC Gorman, and JH Gorman III. Statistical assessment of normal mitral annular geometry using automated three-dimensional echocardiographic analysis. The Annals of thoracic surgery, 97(1):71–77, 2014.

[7] FF Faletra, LA Leo, VL Paiocchi, A Caretta, GM Viani, SA Schlossbauer, S Demertzis, and SY Ho. Anatomy of mitral annulus insights from non-invasive imaging techniques. European Heart Journal-Cardiovascular Imaging, 20(8):843–857, 2019.

[8] A Restivo, G Piacentini, S Placidi, C Saffirio, and B Marino. Cardiac outflow tract: a review of some embryogenetic aspects of the conotruncal region of the heart. The Anatomical Record Part A: Discoveries in Molecular, Cellular, and Evolutionary Biology: An Official Publication of the American Association of Anatomists, 288(9):936–943, 2006.

[9] F Bajolle, S Zaffran, RG Kelly, J Hadchouel, D Bonnet, NA Brown, and ME Buckingham. Rotation of the myocardial wall of the outflow tract is implicated in the normal positioning of the great arteries. Circulation research, 98(3):421–428, 2006.

[10] DA Goor, R Dische, and CW Lillehei. The conotruncus: I. its normal inversion and conus absorption. Circulation, 46(2):375–384, 1972.

[11] HH Nam, PV Dinh, A Lasso, C Herz, J Huang, A Posada, AH Aly, A M Pouch, S Kabir, J Simpson, et al. Dynamic annular modeling of the unrepaired complete atrioventricular canal annulus. The Annals of Thoracic Surgery, 113(2):654–662, 2022.

[12] E Kaza, GR Marx, AK Kaza, SD Colan, H Loyola, DP Perrin, and PJ Del Nido. Changes in left atrioventricular valve geometry after surgical repair of complete atrioventricular canal. The Journal of Thoracic and Cardiovascular Surgery, 143(5):1117–1124, 2012.

[13] T Cong, J Gu, AP Lee, Z Shang, Y Sun, Q Sun, H Wei, N Chen, S Sun, and T Fu. Quantitative analysis of mitral valve morphology in atrial functional mitral regurgitation using real-time 3-dimensional echocardiography atrial functional mitral regurgitation. Cardiovascular Ultrasound, 16(1):1–10, 2018.

[14] A. Goriely. Twisted elastic rings and the rediscoveries of michell's instability. Journal of Elasticity, 84:281–299, 2006.

[15] AL Xavier Jr. Static kirchhoff rods under the action of external forces: Integration via runge-kutta method. Journal of Computational Methods in Physics, 2014, 2014.

[16] S Bartels and P Reiter. Numerical solution of a bending-torsion model for elastic rods. Numerische Mathematik, 146(4):661–697, 2020.

[17] A Goriely and M Tabor. Nonlinear dynamics of filaments i. dynamical instabilities. Physica D: Nonlinear Phenomena, 105(1-3):20–44, 1997.

[18] DJ Steigmann and MG Faulkner. Variational theory for spatial rods. Journal of Elasticity, 33(1):1–26, 1993.

[19] GL van Rijk-Zwikker, BJ Delemarre, and HA Huysmans. Mitral valve anatomy and morphology: relevance to mitral valve replacement and valve reconstruction, 1994.

[20] SY Ho. Anatomy of the mitral valve. Heart, 88(suppl 4):iv5–iv10, 2002.

[21] PP Mishra, MP Rao, V Paranjape, JP Kulkarni, et al. Morphometry of mitral valve. Medical Journal of Dr. DY Patil University, 7(5):625, 2014.

[22] LA Du Plessis and P Marchand. The anatomy of the mitral valve and its associated structures. Thorax, 19(3):221, 1964.

[23] H Muresian, M Diena, G Cerin, and F Filipoiu. The mitral valve: New insights into the clinical anatomy. Maedica, 1:80–87, 2006.

[24] L Taber. Biomechanics of growth, remodeling, and morphogenesis. Appl. Mech. Rev., 48(8):487–545, 1995.

[25] D Ambrosi and F Guana. Stress-modulated growth. Mathematics and mechanics of solids, 12(3):319–342, 2007.

[26] KS Arun, TS Huang, and SD Blostein. Least-squares fitting of two 3-d point sets. IEEE Transactions on Pattern Analysis and Machine Intelligence, PAMI-9(5):698–700, 1987.

[27] NJ Higham. Matrix nearness problems and applications. In M.J.C. Gover and S. Barnett, editors, Applications of Matrix Theory, pages 1–27. Oxford University Press, 1989.

[28] H Alt and M Godau. Computing the fréchet distance between two polygonal curves. International Journal of Computational Geometry & Applications, 5(01n02):75–91, 1995.

[29] PW Alford, JD Humphrey, and LA Taber. Growth and remodeling in a thick-walled artery model: effects of spatial variations in wall constituents. Biomechanics and modeling in mechanobiology, 7:245–262, 2008.

[30] A Ramasubramanian, KS Latacha, JM Benjamin, DA Voronov, A Ravi, and LA Taber. Computational model for early cardiac looping. Annals of biomedical engineering, 34:1355–1369, 2006.

[31] G Bevilacqua, P Ciarletta, and A Quarteroni. Morphomechanical model of the torsional c-looping in the embryonic heart. SIAM Journal on Applied Mathematics, 81(3):897–918, 2021.